

Experimental validation of a thermoelastic model for SMA hybrid composites

Travis L. Turner*
NASA Langley Research Center

ABSTRACT

This study presents results from experimental validation of a recently developed model for predicting the thermomechanical behavior of shape memory alloy hybrid composite (SMAHC) structures, composite structures with an embedded SMA constituent. The model captures the material nonlinearity of the material system with temperature and is capable of modeling constrained, restrained, or free recovery behavior from experimental measurement of fundamental engineering properties. A brief description of the model and analysis procedures is given, followed by an overview of a parallel effort to fabricate and characterize the material system of SMAHC specimens. Static and dynamic experimental configurations for the SMAHC specimens are described and experimental results for thermal post-buckling and random response are presented. Excellent agreement is achieved between the measured and predicted results, fully validating the theoretical model for constrained recovery behavior of SMAHC structures.

Keywords: Shape memory alloys, Nitinol, embedded actuators, hybrid composites, nonlinear thermoelasticity, thermal buckling, thermal post-buckling, random response

1. INTRODUCTION

Shape memory alloys (SMAs) have been the subject of active research for over three decades due to their many unique attributes and the resulting potential for a variety of applications. Early work focused on alloy characterization and discovery of the micromechanics causing the unique properties. A variety of applications ranging from self-erecting structures and energy-conversion devices to thermally actuated fasteners and biomedical devices were also identified in this early effort. Metallurgical work in recent years has seen significant growth, partly due to a substantial increase in applications research that has been stimulated by interest from the biomedical and smart materials communities. Recent smart materials and structures work has shown that SMAs have significant potential for vibration, structural acoustic, and structural shape control applications. Birman¹ published a comprehensive review of the work performed in the areas of SMA constitutive modeling and applications. Several compilations of papers have also been published on the topic, most recently by Otsuka and Wayman², which give a good overview of the alloy characteristics and applications.

Some attributes of SMAs and of the shape memory effect (SME) are shown schematically in Figures 1 and 2. Figure 1 illustrates the martensitic fraction of a SMA as a function of temperature. A simplified depiction of the martensitic and austenitic crystalline structures, and two thermomechanical paths between them, is shown in Figure 2. SMAs exist in a highly ordered (usually cubic) crystalline structure in the high-temperature austenitic state. Martensite resides at low temperature, which has a microstructure with a much lesser symmetry. The martensitic transformation can be temperature or stress induced depending upon the state of the alloy. The solid phase of the material can be transformed by temperature changes without macroscopic deformation, i.e., thermal strains of "normal" magnitudes. However, a SMA can be easily deformed (up to 8% without inducing significant dislocations) due to martensite variant reorientation in the low-temperature martensitic state. The material reverts to the unique cubic structure upon return to the austenitic state at high temperature, which causes recovery of the deformation induced in the martensite (free recovery). If the alloy is prevented from recovering the deformation (constrained recovery) a large tensile recovery stress is developed. A condition in which the alloy performs work, deforms under load, is termed restrained recovery. Although there are many ways in which these alloys can be used, it is the constrained recovery stress effect that is of interest for this study.

The SME has been employed for various applications since its discovery, some of which were mentioned previously. A new class of applications was developed when Rogers and Robertshaw³ introduced the idea of embedding SMA actuators in a composite laminate for structural control. A structure of this type has been termed a shape memory alloy hybrid composite

* t.l.turner@larc.nasa.gov; phone 757 864-3598; fax 757 864-8823; Structural Acoustics Branch, Mail Stop 463, Hampton, VA 23681-2199

(SMAHC). Paine and Rogers published a review of SMAHCs and their applications⁴. Two methods have been proposed for integrating SMA actuators into a composite; bonding the actuators within the composite matrix as a constituent and embedding the actuators within sleeves through the laminate. The work presented in this study focuses on the former method, where prestrained actuators are bonded within the composite matrix and the boundaries of the structure serve also as mechanical restraints for the actuators. Recent work has considered SMAHC structures for static and dynamic structural response control. Frequency response limitations of the SMA (dictated by thermal energy management) have often been cited as an obstacle for dynamic control. However, there are many applications in which a naturally occurring elevated thermal environment can be used to activate the SMA autonomously. The activated SMA actuators act against the mechanical boundaries to adaptively stiffen the structure without control electronics or auxiliary power.

A thermomechanical model was recently developed to study the static and dynamic response of such SMAHC structures⁵⁻⁷. The goals of this study are to present experimental results from static and dynamic tests of SMAHC beam specimens for validation of the theoretical model and for control performance demonstration. Details of the hardware and processes involved in fabrication of the SMAHC specimens and thermomechanical characterization of the constituent materials are given elsewhere^{5,6,8}.

2. MODEL FORMULATION

A brief description of the previously mentioned thermomechanical model is given in this section. Both the constitutive model and resulting equations governing the static and dynamic response of plate-type structures to thermal and mechanical loads are presented.

2.1 Constitutive Modeling

Several constitutive models have been proposed for SMAs⁹⁻¹². These models are not easily used in practice because they are qualitative in nature. Consequently, related micromechanical constitutive models for SMAHC material systems^{13,14} have not been experimentally verified and no model has been available for broad use by the research and engineering communities. An alternative approach is to employ a constitutive model that makes use of experimental measurement of fundamental engineering properties. This type of model is more amenable to incorporation in general structural analysis tools. A constitutive model of this latter type was recently developed and forms the theoretical basis of this study. This model casts the uniaxial thermoelastic constitutive relation for a SMA actuator, along the axis of the actuator, in terms of an effective coefficient of thermal expansion (CTE):

$$\sigma_1 = E[\epsilon_1 - \int_{T_0}^T \alpha_1(\tau) d\tau] \quad (1)$$

where E is the Young's modulus of the SMA, ϵ_1 is the mechanical strain in the 1-direction, and $\alpha_1(T)$ is the "effective" (nonlinear) CTE. Note that this expression is valid for constrained, restrained, or free recovery applications; only the empirical method of obtaining the thermal strain changes. Measurement of the nonlinear CTE over the temperature range of concern would be appropriate for free or restrained recovery applications. For constrained recovery applications, however, one must resort to measurement of the recovery stress and modulus.

It can be shown that, for constrained recovery behavior, the nonlinear thermal strain in Equation (1) can be modeled by linear thermal expansion below the austenite start temperature A_s and can be related to the SMA recovery stress σ_r and modulus by the equation

$$\sigma_r = -E \int_{T_0}^T \alpha_1(\tau) d\tau \quad \text{or} \quad \int_{T_0}^T \alpha_1(\tau) d\tau = -\frac{\sigma_r}{E} \quad (2)$$

at temperatures above A_s . Note that in this case, the nonlinear thermoelastic nature of the SMA is still captured, albeit in a different way, because σ_r and E are temperature dependent and measurements of recovery stress versus temperature are inherently cumulative (integrated). The uniaxial SMA constitutive relation for the transverse direction (2-direction) has a form analogous to Equation (1). However, the transverse CTE $\alpha_2(T)$ is not related to the recovery stress, but is nonlinear due to the differing martensitic and austenitic properties.

There is another interpretation of the relations in equations (1) and (2) that more clearly exhibits the generality and utility of the formulation. One means of implementing this formulation entails forming the functionality of the effective CTE $\alpha_1(T)$

with temperature. In this case, the CTE is positive at temperatures below A_s , it is zero at A_s , and negative at temperatures above A_s . In the presence of mechanical constraints, the resulting thermal stress starts like a conventional linear thermoelastic material, but the compressive stress diminishes at temperatures greater than A_s and becomes tensile as the temperature continues to increase. The thermal stress in the actuator is thus continuous with temperature, but changes sign.

2.2 Governing Equations

The constitutive model for the SMA, described above, was used in a mechanics-of-materials approach to develop the nonlinear thermoelastic constitutive relations for a thin orthotropic SMAHC lamina under conditions of plane stress. These constitutive relations, along with the von Karman strain-displacement relations and classical lamination theory, were used in a variational principle to derive the equations governing the thermomechanical response of a SMAHC panel-type structure subjected to combined steady-state thermal and out-of-plane, dynamic, mechanical loads. The resulting finite element system of equations can be written in the following form

$$\begin{bmatrix} M_b & 0 \\ 0 & M_m \end{bmatrix} \begin{Bmatrix} \ddot{A}_b \\ \ddot{A}_m \end{Bmatrix} + \left(\begin{bmatrix} K_b & K_B \\ K_B^T & K_m \end{bmatrix} - \begin{bmatrix} K_{\Delta T} & 0 \\ 0 & 0 \end{bmatrix} + \frac{1}{2} \begin{bmatrix} N1_b + (N1_b)_B & N1_{bm} \\ N1_{mb} & 0 \end{bmatrix} + \frac{1}{3} \begin{bmatrix} N2_b & 0 \\ 0 & 0 \end{bmatrix} \right) \begin{Bmatrix} A_b \\ A_m \end{Bmatrix} = \begin{Bmatrix} F_b(t) \\ 0 \end{Bmatrix} + \begin{Bmatrix} P_{b\Delta T} \\ P_{m\Delta T} \end{Bmatrix} \quad (3)$$

or

$$[M]\{\ddot{A}\} + ([K] - [K_{\Delta T}] + \frac{1}{2}[N1] + \frac{1}{3}[N2])\{A\} = \{F(t)\} + \{P_{\Delta T}\} \quad (4)$$

where $[M]$ and $[K]$ are the usual system mass and linear stiffness matrices; $[K_{\Delta T}]$ is the geometric stiffness matrix due to the thermal in-plane force vector; $[N1]$ and $[N2]$ are the first- and second-order nonlinear stiffness matrices which depend linearly and quadratically upon displacement $\{A\}$, respectively; $\{F(t)\}$ is the mechanical excitation load vector, and $\{P_{\Delta T}\}$ is the thermal force vector. The subscripts b and m denote bending and membrane components, respectively, and the subscript B indicates that the corresponding stiffness matrix is due to the laminate bending-membrane coupling stiffness matrix $[B]$. Note that the stiffness matrices $[K]$, $[K_{\Delta T}]$, $[N1]$, $[N2]$ and the thermal force vector $\{P_{\Delta T}\}$ are all temperature dependent.

Recall that the applications considered in this study involve immovable in-plane boundaries. This condition leads to a potential for thermoelastic instability. Thus, three types of analyses are required to study the response of structures to thermal and dynamic mechanical loads, governed by Equations (3): (1) thermal buckling analysis, (2) thermal post-buckling analysis, and (3) dynamic analysis. Solutions from these analyses will be shown in section 5 in comparison to experimental measurements. Details of the constitutive model, FE formulation, and solution procedures can be found in related publications⁵⁻⁷.

3. SPECIMEN FABRICATION AND CHARACTERIZATION

A glass-epoxy matrix and Nitinol alloy material system was selected for the SMAHC specimen fabrication effort described in this section. A ribbon form was selected, in lieu of a wire form, as the actuator material to simplify the fabrication procedure, allow for more flexibility in fabrication, and desensitize the actuators to interface voids and stress concentrations.

The previously described FE formulation was used to design candidate specimens for experimental validation of the analytical tool and for performance demonstration. For simplicity, a beam specimen is the focus of this study, but all discussion and results are directly extensible to more practical configurations. Numerical results, along with test hardware and other constraints, led to the beam specimen design shown schematically in Figure 3. The specimen design is by no means optimized, but the predicted performance is in a range that is suitable for the expected loading conditions and to demonstrate significant improvement from the SMA reinforcement. A tooling plate for lay-up and cure of these specimens was designed with knurled clamping restraints at the boundaries to prevent prestrain recovery during cure.

Note that this specimen design calls for a quasi-isotropic lamination $(45/0/-45/90)_{2s}$ with a SMA actuator cross section of $0.0127 \times 1.27 \times 10^{-4}$ m (0.5×0.005 inches) to be embedded within each 0° glass-epoxy layer, i.e., replace a portion of each 0° layer. Material availability and processing limitations dictated a nominal cross section of $0.0023 \times 1.5 \times 10^{-4}$ m (0.09×0.006 inches). This ribbon thickness was considered acceptably close to the estimated glass-epoxy prepreg tape thickness (1.27×10^{-4} m).

m, 0.005 inches) and it was planned that five widths of the ribbon would be placed side-by-side to develop a width near that in the specimen design.

Lengths of the Nitinol ribbon (gage length of 0.635 m, 25 inches) were prestrained 4% (elongated to 0.6604 m, 26 inches) in a servohydraulic test machine prior to laminate fabrication. Widths of the 0° glass-epoxy layers were cut to size during assembly to allow placement of five ribbon widths in discrete strips along the fiber direction. The ends of the Nitinol ribbon were clamped within the knurled grips attached to the tooling plate. The entire assembly was vacuum-bagged and cured in an autoclave according to the glass-epoxy vendor's specifications. Beam specimens were machined from the resulting laminate such that they share a common centerline with the embedded Nitinol strips. Two beam specimens are shown in Figure 4, where it can be seen that one beam has been prepared for installation in a test fixture. The beams have dimensions of 0.5588x0.0254x0.0019 m (22x1x0.078 inches). The SMA leads of the test-prepared beam were trimmed to an overall length of 0.6604 m (26 inches). The overall volume fraction of the SMA within the glass-epoxy dimensions is approximately 13.8%.

The thermomechanical characteristics of the constituent materials must be determined in order to predict the response behavior of these specimens. Tests were performed on glass-epoxy-only specimens to determine the properties of the composite matrix in principal material coordinates (PMC). Tests were performed on uniaxial (0)₂₀ specimens according to ASTM 3039-95a for estimates of the Young's moduli (E_1 and E_2) and Poisson's ratios (ν_{12} and ν_{21}). Similar tests were performed on angle-ply (± 45)₄ specimens according to ASTM 3518-94^{e1} for estimates of the shear modulus (G_{12}). The variation of these properties with temperature is shown in Figure 5. As expected, the fiber direction modulus is fairly constant, but the transverse and shear moduli show some nonlinearity. Specimens for the measurement of the longitudinal and transverse CTE, also in PMC, were machined from the same uniaxial laminate (0)₂₀. Results from these tests are shown in Figure 6, which shows substantial nonlinearity with temperature.

The Nitinol alloy was tested to quantify the recovery stress versus temperature and thermal cycle and the modulus versus temperature. The recovery stress was measured by installing a sample of the Nitinol ribbon with 4% prestrain, remaining from SMAHC specimen fabrication, in a servohydraulic test machine. Samples were subjected to thermal cycles by resistive heating while measuring the force generated as a function of temperature. Representative results showing the average recovery stress versus temperature for thermal cycles 2, 3, 4 and 50 are presented in Figure 7. The Young's modulus of the prestrained ribbon was estimated from tensile test data performed on the test machine using a box furnace. Tests were conducted on 3 ribbon samples at each of 7 temperatures; 21.1°C (70°F), 37.8°C (100°F), 65.6°C (150°F), 79.4°C (175°F), 93.3°C (200°F), 121.1°C (250°F), and 148.9°C (300°F). Modulus estimates from the three samples were averaged and the resulting modulus versus temperature behavior is shown in Figure 8.

Details of the specimen fabrication procedures and of the thermomechanical testing of the constituent materials can be found elsewhere^{5,6,8}. Tabulated data from the thermomechanical tests also appear in those publications.

4. EXPERIMENTAL ARRANGEMENT

All of the experimental results presented in this study result from tests performed on one of the specimens described in the previous section. Static and dynamic tests were performed on the specimen in a clamped-clamped configuration. The static test was conducted to measure the thermoelastic response and demonstrate control of thermal buckling and post-buckling. Dynamic tests were conducted in a base acceleration configuration to measure the random response and demonstrate resonant frequency and broadband dynamic control.

The SMAHC beam specimen is shown mounted in an aluminum fixture in Figure 9. The fixture was designed to provide clamped boundary conditions and an unsupported length of 0.4572 m (18 inches) within the mechanical grips. The fixture was also designed to provide electrical connection and mechanical restraint for the Nitinol ribbon leads protruding from the ends of the SMAHC beam specimens. The mechanical and electrical grips are indicated in the figure by the symbols "m" and "e", respectively. The electrical connections are isolated from the fixture by a layer of fibrous ceramic insulation. The beam is also thermally isolated from the fixture by a layer of this insulation on both sides. The beam is heated by DC electrical current controlled by a thermocouple measurement located approximately on the beam centerline and 0.0127 m (0.5 inch) from the right mechanical grip, indicated in the figure by "tc". The thermal controller consists of a process controller (Omega model CN77353-PV) and a DC power supply (HP model 6652A). Thermocouples also monitor the temperature at each end of the fixture, indicated in Figure 9, and one measures the ambient air temperature.

A rear view of the static experimental configuration is shown in Figure 10, which shows the installation of a laser displacement transducer. The laser displacement transducer (Aromat model LM100) was attached to a three-axis optical positioning traverse and the assembly was mounted in the vicinity of the beam mid-span. The three-axis traverse was used to position the laser impingement position at the beam mid-span and to adjust the laser transducer/beam surface distance to produce zero offset.

A picture of the overall apparatus associated with the base-acceleration tests is shown in Figure 11. The shaker system consists of a large electromechanical shaker configured horizontally and attached to a magnesium slip table, which oscillates in a horizontal plane during operation. The specimen is mounted in the fixture with a vertical orientation to the width-direction in order to drive out-of-plane motion without the effects of gravity. A rear view of the specimen and fixture arrangement is shown in Figure 12, which shows the locations of the dynamic instrumentation. The excitation acceleration is measured by accelerometers (PCB model T352M92) placed at each end of the specimen fixture. The acceleration responses of the beam are measured with accelerometers (Endevco model 2250A-10) at locations 0.10 m (4 inches) and 0.25 m (10 inches) from the right fixture grip in Figure 12, indicated by position numbers 1 and 2, respectively.

It is obvious that the beam response transducers measure the absolute motion of the beam specimens, i.e., including the base motion. Most structural dynamic prediction tools, including the one used in this study, are formulated to provide relative motion response for such configurations. Therefore, it is imperative that experimental procedures allow for the removal of the base motion contributions. The importance is not so much for comparison of peak response amplitude as the base motion is typically much less than that of the flexible structure, but for comparison of frequency response or response spectra off resonance. Base motion removal was performed in this study in the time domain by subtracting the excitation (reference) acceleration from the beam response acceleration.

5. EXPERIMENTAL RESULTS AND MODEL VALIDATION

Experimental results from the static and dynamic test configurations are presented in this section in comparison to responses predicted by the thermomechanical model using the measured material properties and experimental parameters as input.

5.1 Thermoelastic Stability

The SMAHC beam specimen was configured for static thermoelastic testing as described in the previous section. Changes in beam and fixture temperatures during the gripping process and prior to starting the thermal controller were insignificant. The out-of-plane displacement at the mid-span of the beam was measured as it was heated from ambient temperature to 121.1°C (250°F), then allowed to cool naturally to ambient temperature again. Changes in fixture temperatures throughout the duration of the test (~13 minutes) were again insignificant.

The beam was modeled with a 36x2 mesh of 24 degree-of-freedom rectangular plate elements. Element properties were constructed from the appropriate measured material properties described in section 3¹. It was necessary to adjust the boundary conditions in the model to more accurately represent the constraints in the physical system. This will be discussed in more detail in the next subsection. In previous experiments, the temperature distribution generated under these conditions was measured with an infrared thermal-imaging camera. It was found that the temperature distribution was remarkably uniform along the unsupported length of the beam. Therefore, the thermal load was modeled as a uniform temperature distribution.

A comparison between the measured and predicted thermal post-buckling deflection (normalized to the beam thickness) at the beam mid-span is shown in Figure 13. Note that both the measured and predicted deflection exhibit a thermal buckling event at a temperature near ambient. This phenomenon is attributable to the alloy composition and test conditions and relates to the discussion at the end of section 2.1. The material behaves like a conventional linear thermoelastic material at temperatures below A_s and buckles due to thermal expansion, achieving a maximum deflection at a temperature where the Nitinol recovery stress (negative effective CTE) begins to dominate. At higher temperatures, the recovery stress swamps the matrix compressive stress, returning the beam to a flat configuration for the remainder of the test. In general, continued heating can lead to a second instance of thermal buckling because the recovery stress effect saturates (reaches an asymptote)

¹ The thermoelastic stability test constituted thermal cycle number four (4) on the embedded Nitinol ribbon. The appropriate material properties from the tables in reference number 8 were used in the predictions.

while the composite matrix continues to expand. In the present example, the second buckling temperature would be in excess of the epoxy matrix glass-transition temperature (193.3°C, 380°F). These phenomena are described in more detail elsewhere⁵⁻⁷. There it is also shown that thermal buckling can be avoided altogether for such configurations by proper alloy selection, but the example shown here serves as an excellent test-bed for behavior demonstration and model validation.

The predicted post-buckling behavior is in excellent qualitative agreement with the experimental measurement. The main differences between the predicted and measured responses are the slope of the curve from initial buckling to the maximum deflection point, the magnitude of the maximum deflection, and the temperature at which the post-buckling deflection is returned to zero. These discrepancies are attributable to the fact that these systems are extremely sensitive to a multitude of factors including initial deflection, initial stress, boundary conditions, etc. For example, initial deflection in the physical beam is the reason for the more gradual growth of thermal deflection in the experimental results. The discrepancies in peak deflection and deflection elimination temperature are attributable to boundary conditions.

Note that the in-plane boundary conditions are modeled as immovable. Recall that in the physical system the beam extends to the limits of the mechanical grips and the Nitinol leads are terminated beyond that in the electrical grips. Only the ribbon/matrix interface supports the recovery force within the mechanical grip area. The main restraint for the Nitinol is the mechanical termination at the electrical grips. Thus, the compliance of the entire support structure, from one electrical grip to the other, must be considered for accurate modeling of the physical system. It was found that the layer of electrical insulation between the electrical and mechanical grips was the cause for the discrepancies. A compression test was performed on the insulating material and the modulus was found to be less than 137.9 MPa (20 ksi). While the exact stiffness of the boundary would be difficult to quantify, there is no doubt that strain in the insulation is partially relieving the recovery stress and causing a diminished stiffening effect in the physical system. Changes in the model to reflect the compliant in-plane boundaries would move the predicted buckling temperature, peak deflection, and deflection elimination temperature to better agreement with experimental measurement.

5.2 Random Vibration Response

The SMAHC beam specimen was configured for base-acceleration testing as described in the previous section. The beam was excited by random base acceleration over a 10–400 Hz bandwidth with a RMS value of 0.25 g. Time records with an overall length of 200 seconds were collected with a sampling rate of 1024 Hz to allow 50-frame averages with a bandwidth of 0–400 Hz and a frequency resolution of 0.25 Hz. The time data were post-processed to construct relative response quantities, frequency response functions between the beam response transducers and the fixture transducers, and power spectral densities (PSDs) of the acceleration input and relative beam responses. Dynamic data were collected at ambient and at elevated temperatures from 32.2°C (90°F) to 121.1°C (250°F) in 5.6°C (10°F) increments. The beam mechanical and ribbon electrical grip fasteners received a torque of 13.6 N·m (120 in·lbf) just prior to dynamic excitation to minimize effects of changing environmental conditions. The fixture temperature increased by approximately 2.2°C (4°F) during the course of data collection, which was in almost direct proportion to the increase in ambient air temperature.

First, some general observations will be made concerning the experimental behavior and results. Because of the material system characteristics and test configuration, the beam exhibited a thermal post-buckling deflection over a range of temperatures, as described in the previous subsection. The beam exhibited some interesting dynamic behavior (such as intermittent snap-through) within this temperature range, particularly at the point of loss of stability in the flat configuration and then at the point of regaining stability in the flat configuration, as expected. No attempt will be made to predict the dynamic behavior within this range, although it is possible with the present analysis for the portions where the dynamic response is geometrically linear about a nonlinear static deflection. Although the beam was returned to a flat configuration at approximately 54.4°C (130°F), the presented results will focus on higher temperatures. The forced vibration amplitude was visually noticeable in the inactive state (ambient temperature), but was virtually undetectable at temperatures above 71.1°C (160°F). No evidence of delamination or other flaws were detected subsequent to testing, despite the large thermal post-buckling deflection and rather high temperature developed during the tests.

Other observations can be made from a summary of RMS displacement responses and modal parameter estimates shown as a function of temperature in Table 1. The symbols $f_{\#}$ and $\zeta_{\#}$ indicate frequency and critical damping ratio for mode number $\#$, respectively. Temperatures for which the beam was buckled are excluded from the table. The RMS displacements correspond to location 2 and were calculated in the frequency domain from the corresponding accelerometer PSDs. It can be seen that, although a majority of the stiffening effect was achieved at approximately 93.3°C (200°F), performance remains

good far beyond that temperature with a maximum increase in the fundamental frequency of a factor of 5.3 at 121.1°C (250°F). The variation of the modal frequencies with temperature is more easily seen in Figure 14. There, it can be seen that the fundamental frequency starts to reach an asymptotic value at approximately 93.3°C (200°F) and mode three escapes the excitation bandwidth at temperatures above 82.2°C (180°F). Note the peculiar changes in the mode-1 damping near 71.1°C (160°F). This effect is reflected in the measured displacement response RMS values and can be seen in Figure 15, which shows the measured displacement response PSD corresponding to measurement location 2 at ambient and three elevated temperatures. The four PSDs correspond to the filled symbols in Figure 14. It can be seen that the maximum reduction in the RMS displacement response of a factor of 6.4 (-16.2 dB) is achieved at 71.1°C (160°F), where there is maximum peak response reduction due to higher damping, although the stiffening effect continues to increase at higher temperatures. One possible explanation is that there may be an optimal state near 71.1°C (160°F) where there is adequate austenite and dynamic stress and low enough temperature to allow enhanced damping by stress induced martensitic (SIM) transformation hysteresis. At higher temperatures, the dynamic stresses are insufficient to drive the SIM transformation, as it becomes increasingly difficult to induce. Note that at the higher temperatures, where the damping is much lower, large reductions of approximately a factor of 5 (-14 dB) are still achieved.

Recall that the beam dimensions are 0.5588x0.0254x0.0019 m (22x1x0.078 in) with a lamination of (45/0_{sm}/-45/90)_{2s}. Five ribbon widths are embedded within each 0° layer. Each ribbon has a nominal cross section of 2.29e-3x1.52e-4 m (0.09x0.006 inches). This configuration was modeled as a Nitinol volume fraction of 0.5538 in the 0° layers, for an overall volume fraction of 13.8%. The mass densities of the glass-epoxy and Nitinol ribbon (prestrained 4%) were found to be 2.03e+3 kg/m³ (0.19e-3 lbf-s²/in⁴) and 5.72e+3 kg/m³ (0.5349e-3 lbf-s²/in⁴). With the beam and ribbon dimensions, the trimmed ribbon length of 0.66 m (26 inches), and the measured mass densities, the calculated mass of the beam is 75.5e-3 kg (0.166 lbf). This is within 1% of the measured mass of the SMAHC beam, which was found to be 74.92e-3 kg (0.165 lbf).

The element properties for the 32-element-mesh model of the SMAHC beam specimen were evaluated as a function of temperature from the tabulated material properties¹. Modal damping estimates were taken from the experimental data in Table 1. A total of ten modes were used in the predictions in all cases to account for residual effects. The damping was assumed to be 0.1% on all antisymmetric modes and modes out of bandwidth. Although the beam ends are held firmly within the mechanical grips in the physical system, the boundary conditions are not well modeled by perfectly clamped conditions. The combined boundary compliance of the beam and grip assembly resulted in a measured fundamental frequency of 26.4 Hz at ambient temperature. The fundamental frequency with perfectly clamped boundaries was predicted to be 37.6 Hz. Torsional springs with a spring rate of 1.98 N-m/rad (17.5 in-lbf/rad) were applied to the longitudinal-slope degrees of freedom to match the fundamental frequency. The influence of the accelerometers was modeled as lumped masses (~0.4e-3 kg, 2.283e-6 lbf-s²/in) at appropriate nodes. The input acceleration PSDs, as measured by one of the control accelerometers, was taken as input for the predictions.

Measured and predicted displacement PSDs for measurement location 2 on the SMAHC beam at three temperatures are shown in Figures 16–18. The figures show results for ambient temperature, 71.1°C (160°F), and 121.1°C (250°F), respectively, and are representative of the comparisons at all temperatures. The correlation at ambient temperature is excellent with less than 9% difference between measured (3.23 mRMS, 0.0127 inRMS) and predicted (2.96 mRMS, 0.0116 inRMS) RMS response level. The comparisons at elevated temperature show some discrepancy, but are in good qualitative agreement. The predicted responses consistently show slightly higher modal frequencies and lower RMS levels than the corresponding experimental measurements. This trend is due to an over-prediction of the recovery force stiffening effect and is attributable to boundary condition modeling issues described in the previous subsection.

Recall from that discussion that the in-plane boundaries of the physical system are somewhat compliant due to the layer of insulation between the mechanical and electrical grips. The boundary compliance partially relieved the recovery stress and resulted in a reduced stiffening effect. This effect was captured in the model by applying axial springs with a spring rate of 1.97e+6 N/m (11,250 lbf/in) to the in-plane degrees of freedom at the mechanical grips to match the fundamental frequency at 121.1°C (250°F). The effect of fixture expansion with temperature was also modeled by applying appropriate enforced displacements at the ends of the unsupported length of the beam. New predicted responses were made with these changes and are shown in comparison to the measured response PSDs for measurement location 2 on the SMAHC beam in Figures 19–21. It can be seen that excellent agreement is achieved between the predicted and measured responses at all temperatures.

¹ The base-acceleration test constituted thermal cycle number two (2) on the embedded Nitinol ribbon. The appropriate material properties from the tables in reference number 8 were used in the predictions.

6. SUMMARY

A thermomechanical model was recently developed for analyzing the behavior of shape memory alloy hybrid composite (SMAHC) structures. The SMAHC configuration under consideration consists of a composite matrix with embedded SMA actuators that act against the mechanical boundaries of the structure when thermally activated to adaptively stiffen the structure. The model captures the thermal nonlinearity of the SMA and composite matrix, but is macromechanical in nature such that it depends only upon measurement of fundamental engineering properties. Although the model is only exercised for constrained recovery configurations, it is also valid for predicting restrained or free recovery behavior.

A glass-epoxy and Nitinol alloy material system was selected for the specimen fabrication and constituent characterization program. A SMAHC laminate was fabricated from the glass-epoxy matrix with a quasi-isotropic lamination and Nitinol ribbon actuators, with a prestrain of 4%, embedded in discrete 0.011 m (0.45 inch) strips in four (0°) of 16 layers. Beam specimens were machined from the laminate sharing the centerline of the embedded Nitinol strips. The overall volume fraction of the Nitinol is approximately 13.8%. Static and dynamic tests were conducted on a SMAHC beam specimen in a clamped-clamped configuration.

The static test was conducted to measure the thermoelastic response of the beam over a temperature range of ambient to 121.1°C (250°F). A post-buckling deflection occurred at a temperature just above ambient due to the material system selection and testing conditions. At higher temperatures, the thermal post-buckling deflection was eliminated by the overwhelming effect of the Nitinol recovery stress. Good agreement was achieved between the measured and predicted results with existing discrepancies attributable to boundary conditions and experimental imperfections not included in the model.

Dynamic experiments were conducted on the SMAHC beam specimen in a base acceleration configuration. Measurements of the band-limited random response were taken at ambient and elevated temperatures from 32.2°C (90°F) to 121.1°C (250°F) in 5.6°C (10°F) increments. The fundamental frequency of the beam was increased by a factor of 5.3 at 121.1°C (250°F) relative to that at ambient temperature. A maximum RMS displacement response reduction of a factor of 6.4 (-16.2 dB) was achieved at a temperature of 71.11°C (160°F) rather than at the maximum temperature. This was apparently caused by enhanced damping due to stress induced martensitic transformation hysteresis. Nonetheless, similar reductions of around a factor of 5 (-14 dB) were achieved at higher temperatures. It was possible to include all boundary effects in the dynamic response prediction and excellent agreement was achieved between the measured and predicted dynamic response at all temperatures.

The thermomechanical model and solution procedures have been fully validated against the static and dynamic response of a SMAHC beam specimen. The model and fabrication procedures are directly applicable to more practical structures and work is continuing for model validation with experimental results from a sub-component-type structure.

ACKNOWLEDGEMENTS

The author gratefully acknowledges the assistance of Cynthia L. Lach, Craig Ohlhorst (NASA LaRC), William Johnston, Joel Alexa, Stewart Walker, and Harold Claytor (Analytical Services and Materials), Jerry Draper (Lockheed Martin Astronautics), and Kenneth Blount (Materials Research and Engineering) for their help in characterizing the thermomechanical properties of the glass-epoxy and Nitinol materials. Thanks are also due to Scott Wallace (NASA LaRC) and Ravi Shenoy (Analytical Services and Materials) for their assistance in providing differential scanning calorimetry measurements from the Nitinol. The assistance of Roberto Cano and Hoa Luong (NASA LaRC) in specimen fabrication and Howard Jones and Jeff Pierro (NASA LaRC) with static and dynamic testing is also greatly appreciated.

REFERENCES

1. V. Birman, "Review of Mechanics of Shape Memory Alloy Structures," *Appl. Mech. Rev.*, **50(11)**, 629-645, 1997.
2. K. Otsuka and C. M. Wayman (Editors), *Shape Memory Materials*, Cambridge University Press, Cambridge, UK, 1998.
3. C. A. Rogers and H. H. Robertshaw, "Shape Memory Alloy Reinforced Composites," *Engineering Science Preprints 25*, Society of Engineering Science, Inc., ESP25.8027, 1988.
4. J. S. N. Paine and C. A. Rogers, "Review of Multi-Functional SMA Hybrid Composite Materials and their Applications," *Adaptive Structures and Composite Materials: Analysis and Application*, AD-Vol. 45/MD-Vol. 54, 37-45, ASME, 1994.

5. T. L. Turner, "Thermomechanical Response of Shape Memory Alloy Hybrid Composites," Ph.D. Dissertation, Virginia Polytechnic Institute and State University, 2000.
6. T. L. Turner, "Thermomechanical Response of Shape Memory Alloy Hybrid Composites," NASA/TM-2001-210656, 2001.
7. T. L. Turner, "A New Thermoelastic Model for Analysis of Shape Memory Alloy Hybrid Composites," *J. of Intell. Matl. Sys. & Stru.*, To Appear May 2001.
8. T. L. Turner, "Fabrication and Characterization of SMA Hybrid Composites," *Smart Structures and Materials 2001; Active Materials: Behavior and Mechanics*, SPIE Vol. 4333, Paper No. 4333-60, Newport Beach, CA, 2001.
9. K. Tanaka and S. Nagaki, "A Thermomechanical Description of Materials with Internal Variables in the Process of Phase Transformation," *Ingenieur-Archiv*, **51**, 287-299, 1982.
10. C. Liang and C. A. Rogers, "One-Dimensional Thermomechanical Constitutive Relations for Shape Memory Materials," *Journal of Intelligent Material Systems and Structures*, **1**, 207-235, 1990.
11. L. C. Brinson, "One-Dimensional Constitutive Behavior of Shape Memory Alloys: Thermomechanical Derivation with Non-Constant Material Functions," *Journal of Intelligent Material Systems and Structures*, **4**(2), 229-242, 1993.
12. J. G. Boyd and D. C. Lagoudas, "A Thermodynamical Constitutive Model for Shape Memory Materials - Part I: The Monolithic Shape Memory Alloy," *Int. J. of Plasticity*, **12**(7), 805-842, 1996.
13. J. G. Boyd and D. C. Lagoudas, "A Thermodynamical Constitutive Model for Shape Memory Materials - Part I: The SMA Composite Material," *Int. J. of Plasticity*, **12**(7), 843-873, 1996.
14. V. Birman, "Micromechanics of Composites with Shape Memory Alloy Fibers in Uniform Thermal Fields," *AIAA Journal*, **34**(9), 1905-1912, 1996.
15. T. L. Turner, "SMA Hybrid Composites for Dynamic Response Abatement Applications," *7th International Conference on Recent Advances in Structural Dynamics*, **1**, 453-465, ISVR, University of Southampton, Southampton, UK, 2000.
16. T. W. Duerig, K. N. Melton, D. Stockel, and C. M. Wayman (Editors), *Engineering Aspects of Shape Memory Alloys*, Butterworth-Heinemann, Boston, MA, 1990.

Table 1: Summary of the RMS displacements at position 2 in Figure 12 and modal parameters versus temperature.

Temp. °C	RMS Displ. m	f_1 Hz	ζ_1 %	f_3 Hz	ζ_3 %	Temp. °C	RMS Displ. m	f_1 Hz	ζ_1 %	f_3 Hz	ζ_3 %
23	0.322e-3	26.4	0.89	160.3	0.95	87.8	0.063e-3	130.9	0.14	—	—
—	—	—	—	—	—	93.3	0.062e-3	134.0	0.14	—	—
60	0.15e-3	83.1	0.10	279.3	0.45	98.9	0.066e-3	136.0	0.11	—	—
65.6	0.11e-3	94.4	0.13	309.4	0.17	104.4	0.067e-3	137.6	0.11	—	—
71.1	0.05e-3	107.0	0.50	342.7	0.16	110	0.073e-3	139.2	0.10	—	—
76.7	0.063e-3	118.3	0.19	372.5	0.28	115.6	0.072e-3	139.7	0.10	—	—
82.2	0.068e-3	126.7	0.15	—	—	121.1	0.067e-3	140.0	0.09	—	—

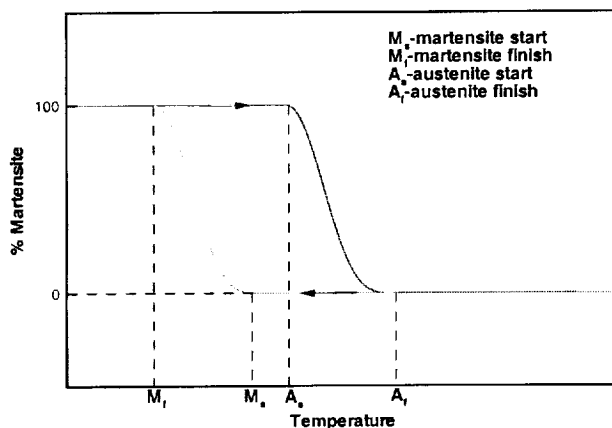


Figure 1: Schematic of martensitic fraction versus temperature, after Liang and Rogers¹⁰.

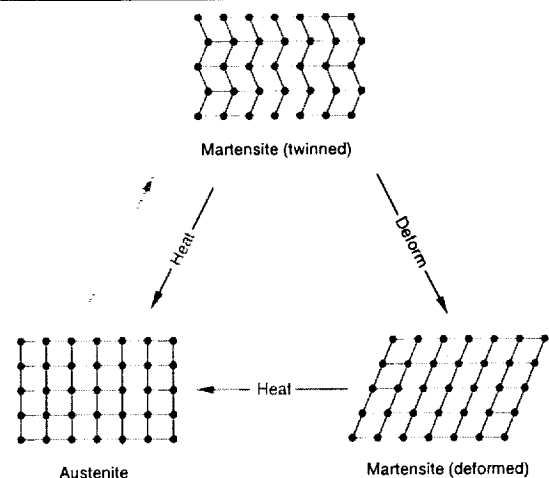


Figure 2: Schematic of the SME, after Wayman and Duerig¹⁶.

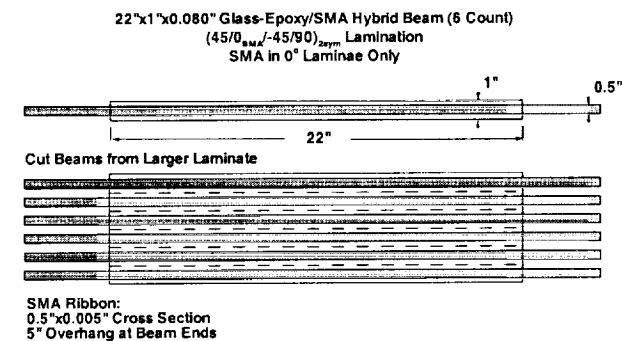


Figure 3: Schematic of SMAHC beam specimen configuration.

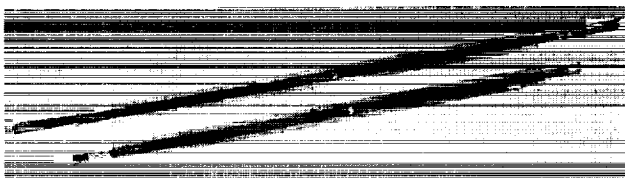


Figure 4: SMAHC beam specimens machined from panel.

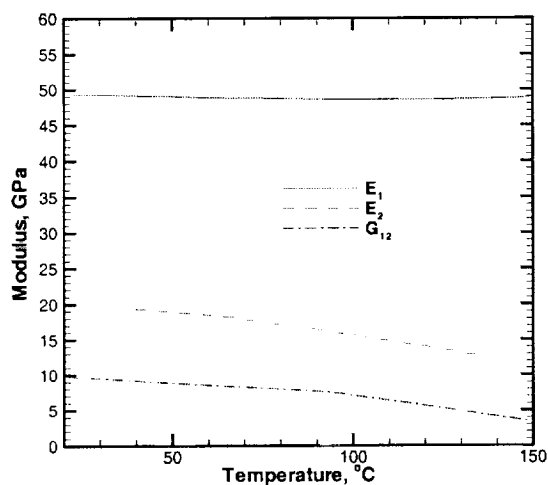


Figure 5: Glass-epoxy moduli versus temperature.

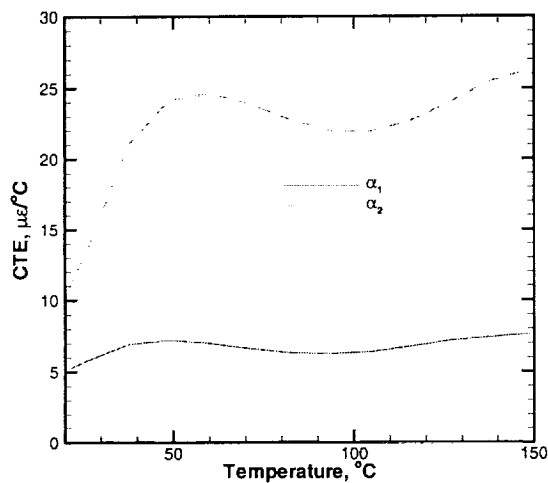


Figure 6: Glass-epoxy CTEs versus temperature.

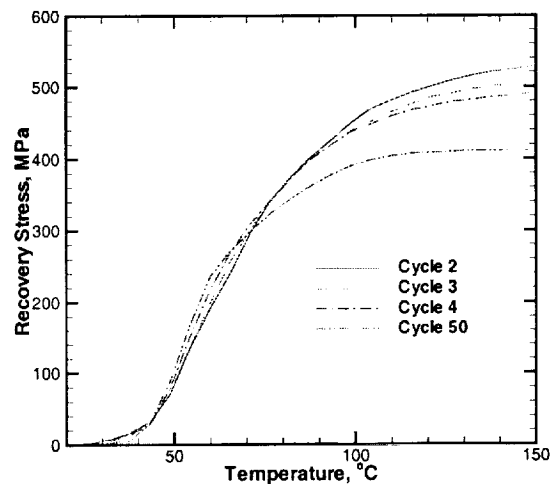


Figure 7: Nitinol average recovery stress versus temperature.

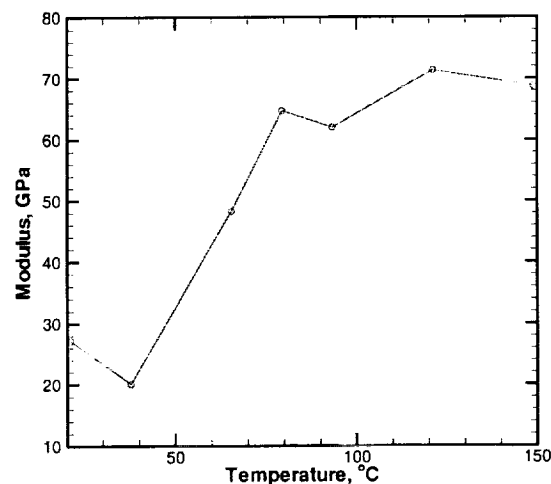


Figure 8: Nitinol modulus versus temperature.

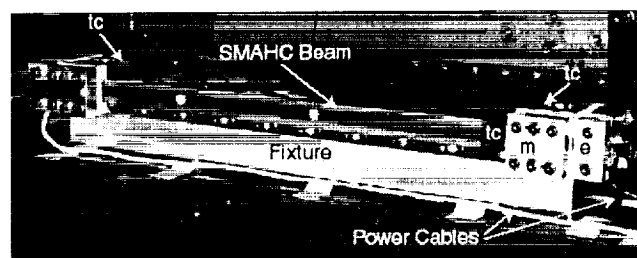


Figure 9: SMAHC beam specimen mounted in support fixture.

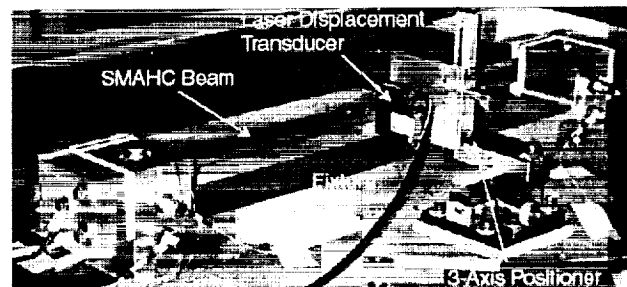


Figure 10: Static thermoelastic experimental configuration.



Figure 11: Overall dynamic experimental configuration.

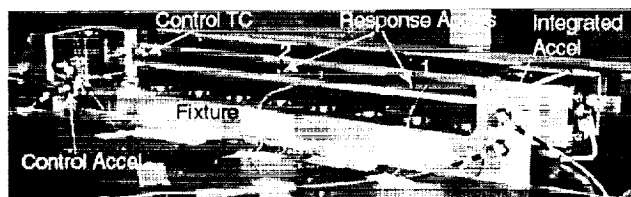


Figure 12: Dynamic experimental configuration.

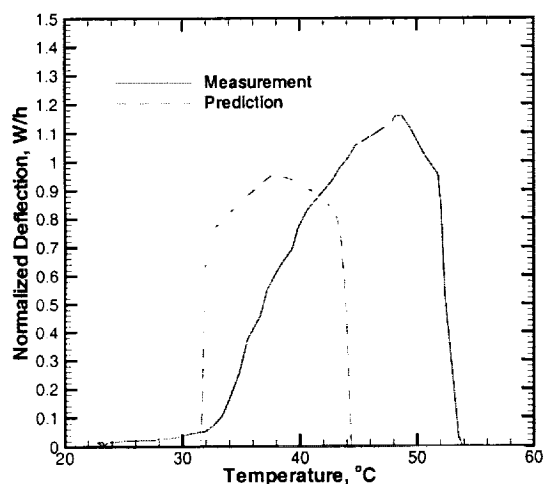


Figure 13: Measured and predicted mid-span, normalized, post-buckling deflection versus temperature.

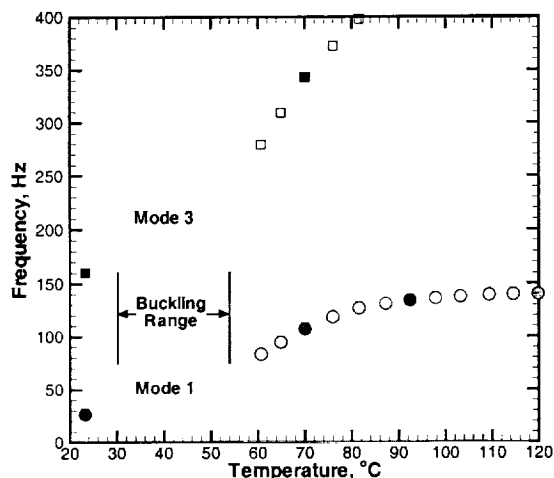


Figure 14: First and third modal frequencies versus temperature.

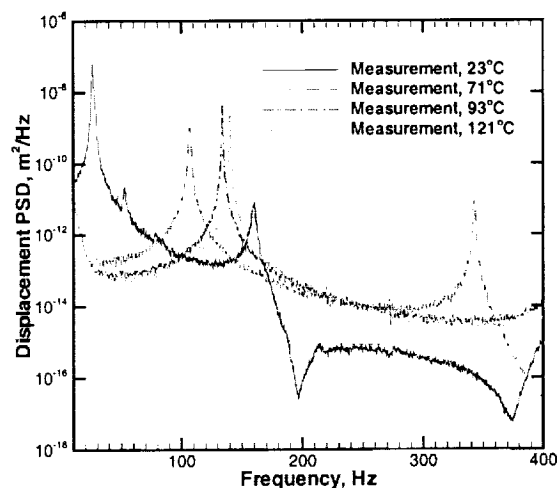


Figure 15: Measured displacement PSDs for position 2 at ambient and elevated temperatures.

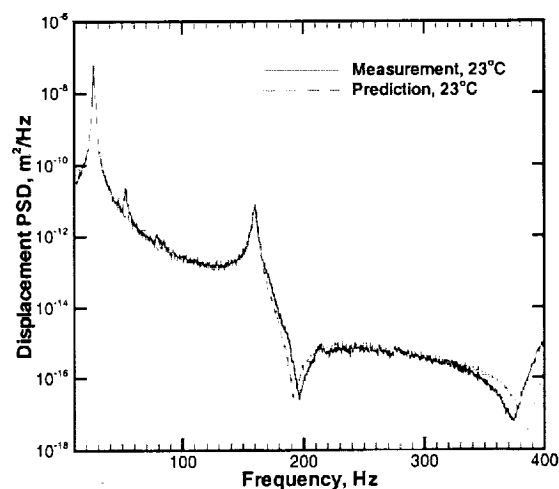


Figure 16: Measured and predicted displacement PSD for position 2 at ambient temperature.

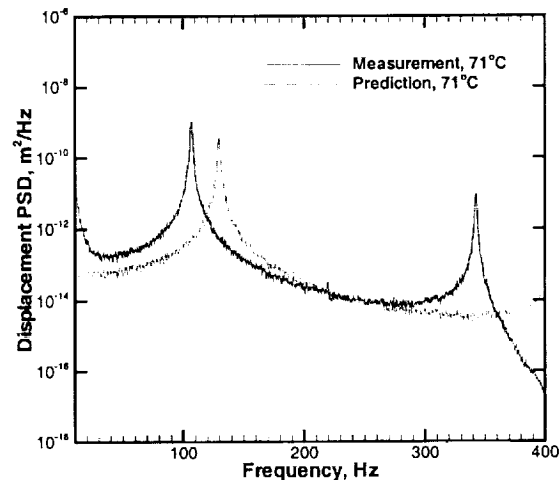


Figure 17: Measured and predicted displacement PSD for position 2 at 71°C (160°F).

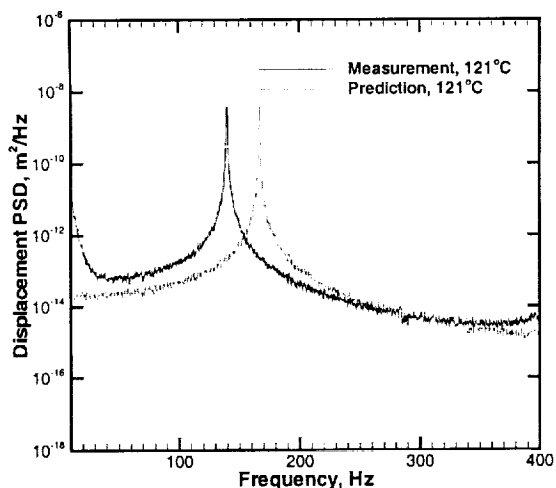


Figure 18: Measured and predicted displacement PSD for position 2 at 121°C (250°F).

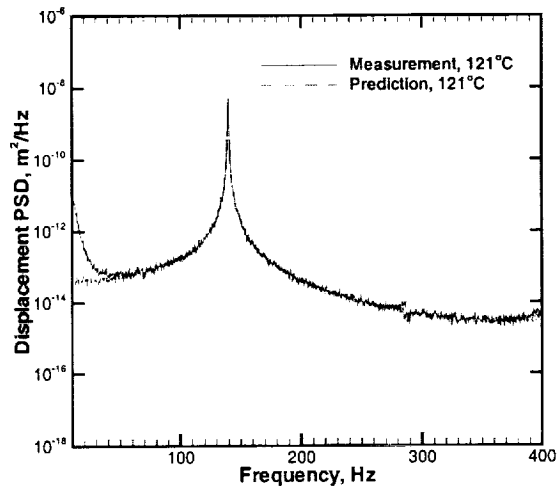


Figure 21: Measured and predicted displacement PSD for position 2 at 121°C (250°F) w/ in-plane boundary effects.

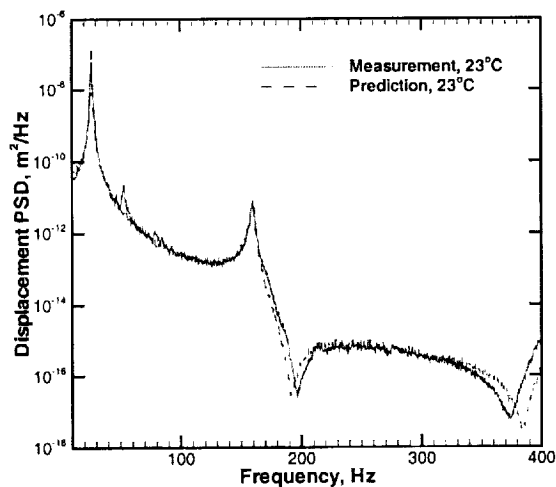


Figure 19: Measured and predicted displacement PSD for position 2 at ambient temperature w/ in-plane boundary effects.

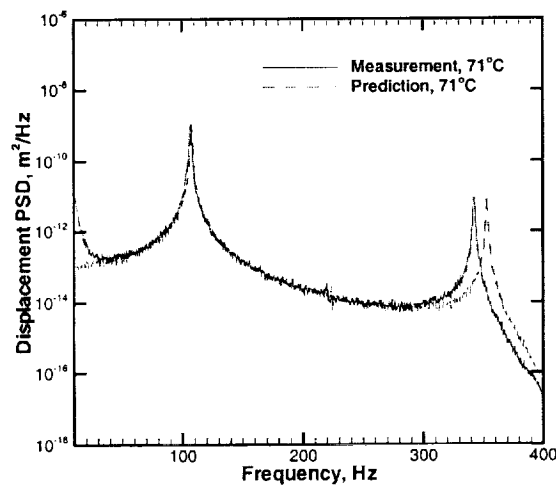


Figure 20: Measured and predicted displacement PSD for position 2 at 71°C (160°F) w/ in-plane boundary effects.